EXPLICIT REPRESENTATION OF CLOUDS AND PRECIPITATION

E. Richard and N. Chaumerliac
Laboratoire de Météorologie Physique
Clermont-Ferrand, France

1. INTRODUCTION

Techniques for simulating cloud and precipitation processes in a numerical model range from the very simple to the very complex. In some situations, it may suffice to merely precipitate out the excess condensate when the relative humidity within a grid volume reaches a predetermined value. Such techniques stand in sharp contrast, however to models which include detailed microphysical processes and which seek to simulate the detailed structure of a thunderstorm cell. While these two examples differ dramatically in their treatment of the cloud and precipitation processes, they nevertheless possess a common characteristic: they explicitly treat the microphysical processes on the resolvable grid scale that is inherent in the model.

Although explicit techniques may cover a wide range of complexity, they differ in fundamental manner from procedures which implicitly deduce the cloud and precipitation fields from other meteorological fields explicitly represented in the model. On the meso-α or β scale, the relationship between the explicit and implicit treatment of clouds and precipitation processes is often likened to the relationship between stratiform and cumuliform clouds. And indeed, the concept of cumulus parameterization postulates the presence and properties of clouds whose horizontal dimensions are too small to be resolved by the model.

It is important to note that even explicit treatments of precipitation associated with grid resolvable stratiform clouds contain parameterization of subgrid scale mixing processes. One important issue to be addressed is the scale at which such conventional treatment no longer suffices and one must resort to an implicit treatment of subgrid scale convective processes.

Contradictory results have been reported in the literature for α mesoscale models. For instance, Ross and Orlanski (1982) and Hsie et al. (1984) explicitly simulated frontogenesis processes using respectively grid size of 61.5 km and 40 km. Their simulations favour the use of the explicit approach. By contrast, for the simulation of an

observed mesoscale convective complex, Molinari and Dudek (1986) with a similar grid resolution showed that an explicit simulation produced localized excessive rainfall, due to grid size instability and interpreted by Zhang et al. (1988) as unrealistic developments of the conditional instability of the second kind.

On the β mesoscale, where the saturation delay problem is reduced and where the updraft/downdraft strength approaches closer to values observed in nature, the explicit approach has been thought of potential value. However Zhang et al. (1988) with a grid size of 12.5 km found than the best simulation of the 77 Johnstown flash flood event was obtained when a semi-implicit (i.e. a prognostic explicit scheme + an implicit convective scheme) was used. Even though an explicit approach cannot be expected to provide an adequate depiction of the precipitation process associated with deep severe convection on the α mesoscale, its incorporation into a mesoscale model is necessary in order to reproduce certain types of precipitating weather systems.

In the sections which follow, we briefly summarize the essential features of the microphysical processes used in our explicit treatment of clouds and precipitation. We then present several specific examples to illustrate the ability of the model to provide an adequate description of the clouds and precipitation on the β and α mesoscale.

2. TYPES OF EXPLICIT REPRESENTATION

The term explicit approach covers a range of microphysical parameterizations in numerical mesoscale models. In the simplest form to be referred to as "instant rainout", any liquid water is assumes to rain out instantly after condensation. No cloud stage is included and there is no evaporation and no water loading. Due to its attractive simplicity, numerous studies have employed this approach in numerical weather prediction models (Anthes et al., 1983; Molinari and Dudek, 1986). However this very simple method is highly prone to instability and is recognized to yield localized excessive rainfall.

In a second type of explicit representation, a cloud water prediction equation is incorporated including rates of condensation, evaporation and eventually conversion of cloud to rainwater. The cloud water produced by condensation is advected and evaporates when encountering subsaturation. The conversion of cloud to rainwater is determined by the excess of cloud water over some critical value taken from 0.55 gkg^{-1} (Hsie and Anthes, 1984) to 1.5 gkg^{-1} (Ross and Orlanski, 1982). A simple water loading effect is incorporated by using a liquid water virtual temperature in

the hydrostatic equation. In this representation, rainwater (if included) once formed, is again assumed to fall instantaneously.

A third type of explicit representation incorporates an additional prediction equation for rainwater (Hsie et al., 1984). The assumption of instantaneous rainwater fallout is replaced by an assumed terminal velocity and such processes as rain evaporation and accretion of cloud droplets by rain are taken into account. Incorporation of more realistic physics such as both resolvable scale evaporation and hydrostatic water loading makes this type III formulation less sensitive to the instability problem mentioned above.

3. PARAMETERIZATIONS USED IN THE SALSA MODEL

SALSA is a numerical hydrostatic model (Nickerson et al., 1986) which can be run on α or β mesoscale. It includes a detailed explicit representation of the microphysics which belongs to the third type in the above classification. The predicted thermodynamic variable are H, an entropy variable defined by $H = Ln(T/\hat{p}) + L_v q_v / C_p T$, and q a moisture variable defined as the sum of the vapor mixing ratio q_v and the cloud water mixing ratio q_{cw}. Temperature and cloud water mixing ratio are not explicitly predicted by the model but are diagnosed from the predicted value of H and q. In the event of supersaturation with respect to liquid water, excess of vapor is converted into cloud water. Liquid water in the model is partitioned into two categories: rainwater, which falls through the air; and cloud water which wafts around with the air. In the model, two different parameterizations can de used to described the liquid water evolution, the one is a Kessler type parameterization (Kessler, 1969), the other is based upon Berry and Reinhardt 's work (Berry and Reinhardt, 1974a,b).

3.1 Description of the parameterizations

In the Berry and Reinhardt parameterization (BR), rainwater is assumed to be distributed lognormally with diameter; that is,

$$dN_{rw} = \frac{N_{rw}}{\sqrt{2\pi}\sigma_r D} exp\Big[- \frac{1}{2\sigma_r^2} ln^2\big(\frac{D}{D_{or}}\big)\Big] dD \qquad (1)$$

is the number of raindrops in the size range D to $D + dD$, and N_{rw} is the total number of raindrops. Here σ_r and D_{or} are distribution parameters.

If the diameter D_{or} is large enough so that cloud-size droplets contribute very little to the total number concentration, the integration of (1) over the entire spectrum of

drops of mass $\pi\rho_w D^3/6$ yields the following expression for q_{rw} the rainwater mixing ratio:

$$q_{rw} = \frac{N_{rw}}{\rho_a}\left(\frac{\pi}{6}D_{or}^3\rho_w\right)exp\left(\frac{9}{2}\sigma_r^2\right) \tag{2}$$

where ρ_a and ρ_w represent the density of air and liquid water respectively.
Extensive use of the work of Berry and Reinhardt (1974a,b) has been made in developing parameterization for autoconversion, accretion and self-collection processes appropriate to the log normal raindrop distribution. Separate prognostic equations are written for both rainwater mixing ratio and total number concentration. This leads to the following set of equations:

$$\frac{dq}{dt} = -AU(Q) - AC(Q) + EV(Q) + Fr(Q) \tag{3}$$

$$\frac{dq_{rw}}{dt} = AU(Q) + AC(Q) - EV(Q) + SE(Q) \tag{4}$$

$$\frac{dN_{rw}}{dt} = AU(N) - EV(N) - SC(N) + SE(N) \tag{5}$$

AU, AC, SC, EV and SE designates respectively the autoconversion, accretion, self-collection, rain evaporation and sedimentation rates. This detailed expression of these terms may be found in Richard et Chaumerliac, 1989. Let us note however that self-collection (coalescence of raindrops among themselves) affects only the concentration of raindrops while accretion affects only the mixing ratio. And although the accretion and autoconversion process represent source terms in the rainwater equations, they are at the same time sink terms for cloud water and are therefore incorporated into the prognostic equation of q.
The Kessler type parameterization (K) makes use of a Marshall-Palmer distribution for the raindrops. The number of raindrops whose diameter lies in the interval D to $D + dD$ is given by

$$dN_{rw} = N_o exp(-\lambda D)dD. \tag{5}$$

This formulation originally derived by Marshall and Palmer (1948) has been widely used. Observations from Waldvogel (1974) for different types of rain show a range of values for N_o from 0.4 10^7 m^{-4} to 3.5 10^7 m^{-4}. The total mass of precipitation per unit volume is obtained by multiplying the distribution given in (5) by the mass of one raindrop of diameter D and by integrating over all diameters, i.e.,

$$\rho_a q_{rw} = \int_0^\infty \frac{\pi}{6}\rho_w D^3 N_o exp(-\lambda D)dD = \frac{\pi\rho_w N_o}{\lambda^4}. \tag{6}$$

In the Kessler parameterization, rainwater is predicted solely by its mixing ratio q_{rw}. The set of microphysical equations, with the same notations than above, is then the following:

$$\frac{dq}{dt} = -AU(Q) - AC(Q) + EV(Q) + Fr(Q) \tag{7}$$

$$\frac{dq_{rw}}{dt} = AU(Q) + AC(Q) - EV(Q) + SE(Q) \tag{8}$$

In both parameterizations, there are more parameters in the raindrop distributions than predictive variables, therefore for each distribution, one of these unknown parameters must be specified. The effects of varying these parameters are illustrated in Fig.1, which presents mass density functions for a given rainwater content of 0.5 g m^{-3}, as a function of raindrop diameter. Figure 1a corresponds to the Marshall-Palmer distribution for various values of N_o, Figure 1b corresponds to the log-normal distribution for three values of σ_r and a given number concentration N_{rw}. The variation of N_o over the whole range of measured values has little effect on the mass density function. A slight shift towards larger diameters is observed when N_o is decreased but the peak value and the shape of the curves remain the same. Therefore, in the following, N_o will be set equal to 10^7 m^{-4}. A quite different behavior is found in Fig.1b. The mass density function is much more sensitive to changes in σ_r. A decrease in σ_r both reduces the peak value and broadens the spectrum. The value $\sigma_r = 0.547$ is then retained providing the log-normal distribution with the most similar spectrum both in shape and amplitude to the Marshall-Palmer distribution. In the Kessler parameterization, it is now possible to compute the other parameter λ as a function of N_o and q_{rw} (cf equation(6)). In the same way, D_{or} in the BR parameterization can be expressed as a function of σ_r, q_{rw} and N_{rw} (cf equation(2)). One of the major advantages in the BR parameterization is the prediction of N_{rw}, which allows much more flexibility in the representation of the raindrop spectrum. As an example, for a fixed value of the rainwater content, log-normal mass density functions have been drawn in Fig.2 for three predicted values of the number concentration and compared with the corresponding function for Marshall-Palmer. Depending on the predicted value of the concentration, the BR spectrum is centered on small diameter (500 μm) or on large diameter (1000 μm), while the K spectrum remains centered on the same (large) diameter. The shift of the spectrum towards larger diameter, in the case of Kessler can be achieved only by increasing the rainwater mixing ratio, while in the case of BR it can also result from decreasing the number concentration. Therefore, the prediction of the number concentration combined with a log-normal

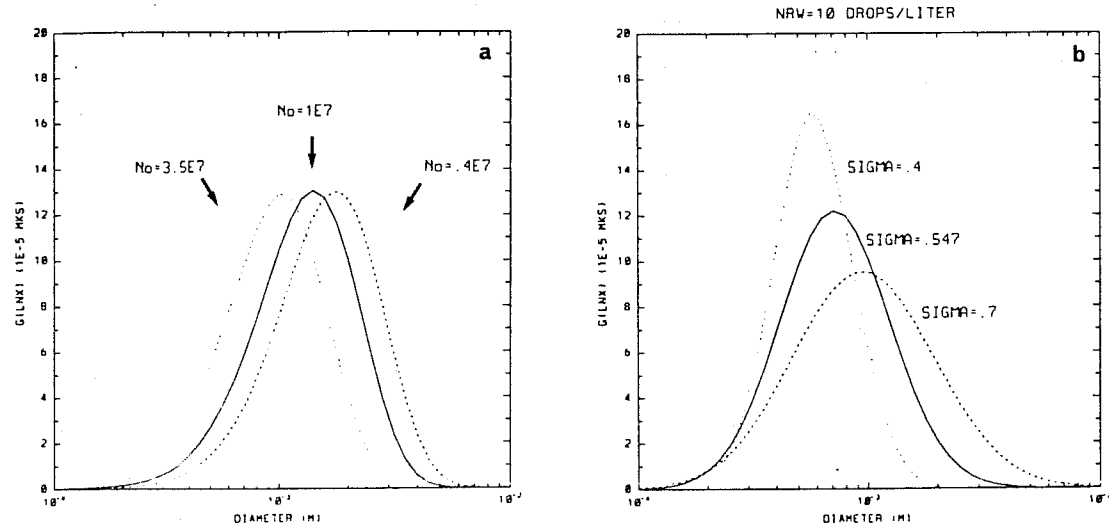

Fig.1 Mass density functions for a given rainwater content of $0.5gm^{-3}$ as a function of raindrop diameter: (a) for Marshall-Palmer distribution for three values of N_o, expressed in m^{-4}, (b) for log-normal distribution for three values of σ_r and $N_{rw} = 10$ drops per liter.

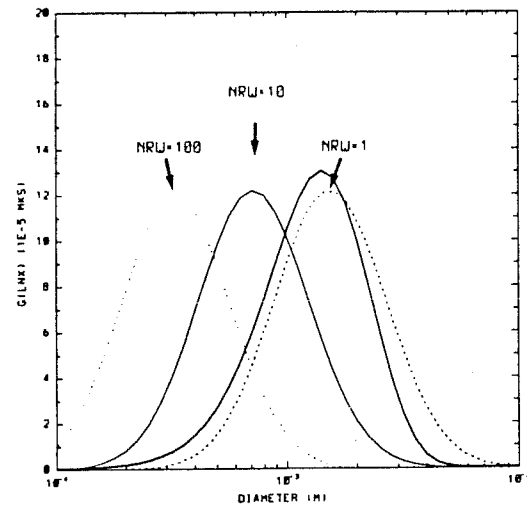

Fig.2 Mass density functions for a given rainwater content of $0.5gm^{-3}$ obtained with the log-normal distribution for $\sigma_r = 0.547$ and three predicted values of N_{rw} in drops per liter (thin lines) and with the Marshall-Palmer distribution for $N_o = 10^7 m^{-4}$ (thick line).

distribution brings an additional degree of freedom which provides more detailed information about the raindrop size spectrum and facilitates the representation of the physical processes which control the evolution of the spectrum (Feingold and Levin, 1986).

3.2 Comparison and test of the parameterizations

3.2.1 Orographic cloud

Simulations have been performed with a two-dimensional version of the model over a horizontal domain of 430 km with a grid mesh of 10 km. The vertical domain extends from the ground to 100 mb and is discretized into 15 equally spaced levels in the vertical coordinate ν (where ν is a modified σ vertical coordinate). Lateral boundary conditions are of the Davies type (Davies, 1983). At the upper boundary, a top absorbing layer occupies the first five vertical levels. The simulation duration is 6 h with a time step of 10 s. The planetary boundary layer is parameterized according to O'Brien (1970) with a constant depth of 1 km.

A meteorological scenario of a mountain wave has been selected in order to provide a well defined forcing mechanism as well as a dynamical and thermodynamical consistent setting for the production of clouds and precipitation (Durran and Klemp, 1983; Chaumerliac et al., 1987). The model is run over an idealized bell-shaped mountain, 1 km high and 20 km in halfwidth. The initial atmosphere consists in a layer of constant lapse rate with 80% relative humidity up to 250 mb, which is topped by a dry isothermal layer. The initial horizontal windspeed is 20 ms^{-1}.

For this orographic rain situation, results obtained both from K and BR are systematically compared. BR results are presented for the two values of the autoconversion coefficient bracketing the Kessler autoconversion rate and will now be referred to as BR1 and BR2. In Fig.3, vertical cross-sections of cloud water mixing ratios, rainwater mixing ratios and precipitation rates have been reported for K, BR1 and BR2. Cloud water fields (Fig.3a) are comparable for K and BR2 whereas cloud water mixing ratios obtained with BR1 are weaker due to a more efficient conversion from cloud to rain. The precipitation rates of K and BR2 (Fig.3c) are also comparable in intensity but differ slightly in their spatial extent. Surprisingly, the corresponding rainwater mixing ratios (Fig.3b) are quite different. BR2 produces much larger rainwater mixing ratios than K. Further insight may be obtained from Fig.4 which shows mass density functions for K, BR1 and BR2 for various model grid points in the vicinity

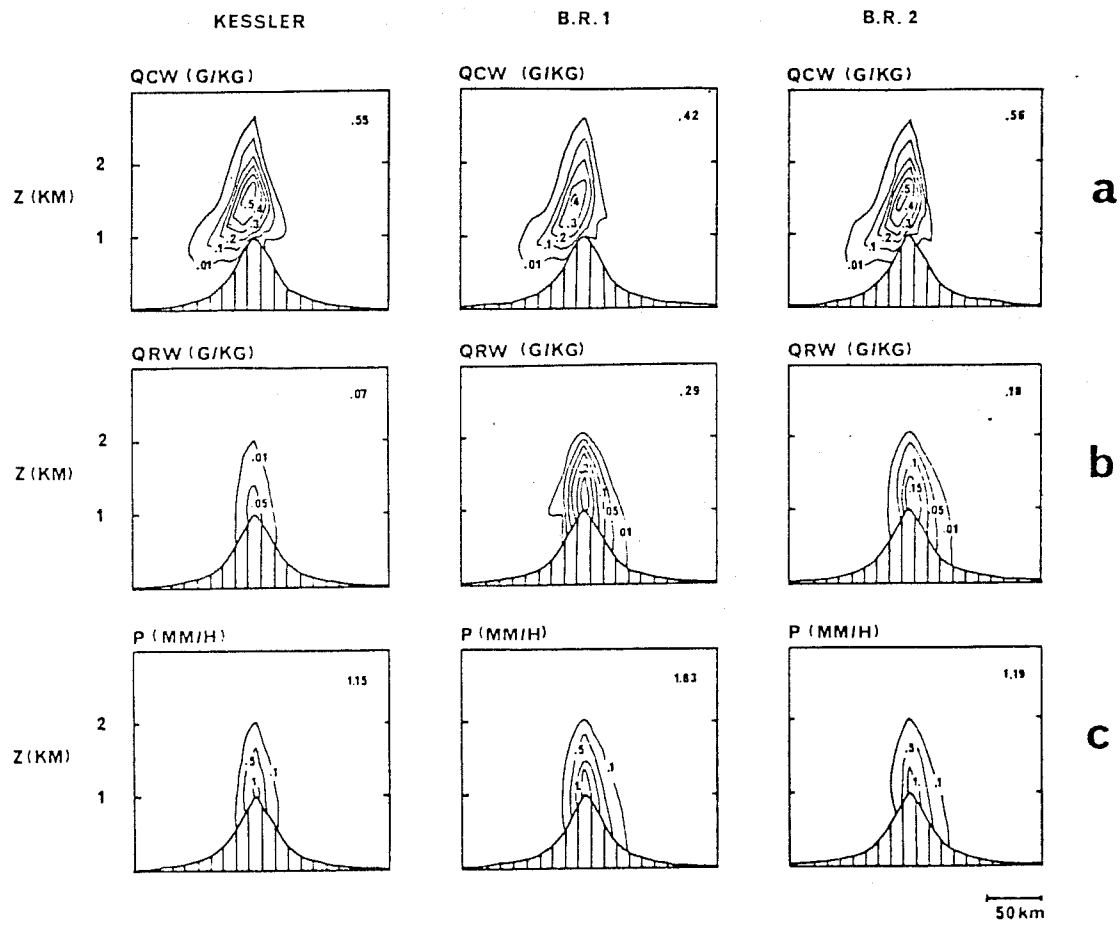

Fig.3 Vertical cross section of cloud water mixing ratios, rainwater mixing ratios and precipitation rates for K, BR1 and BR2. Maximum values are given in the upper right corner of each figure.

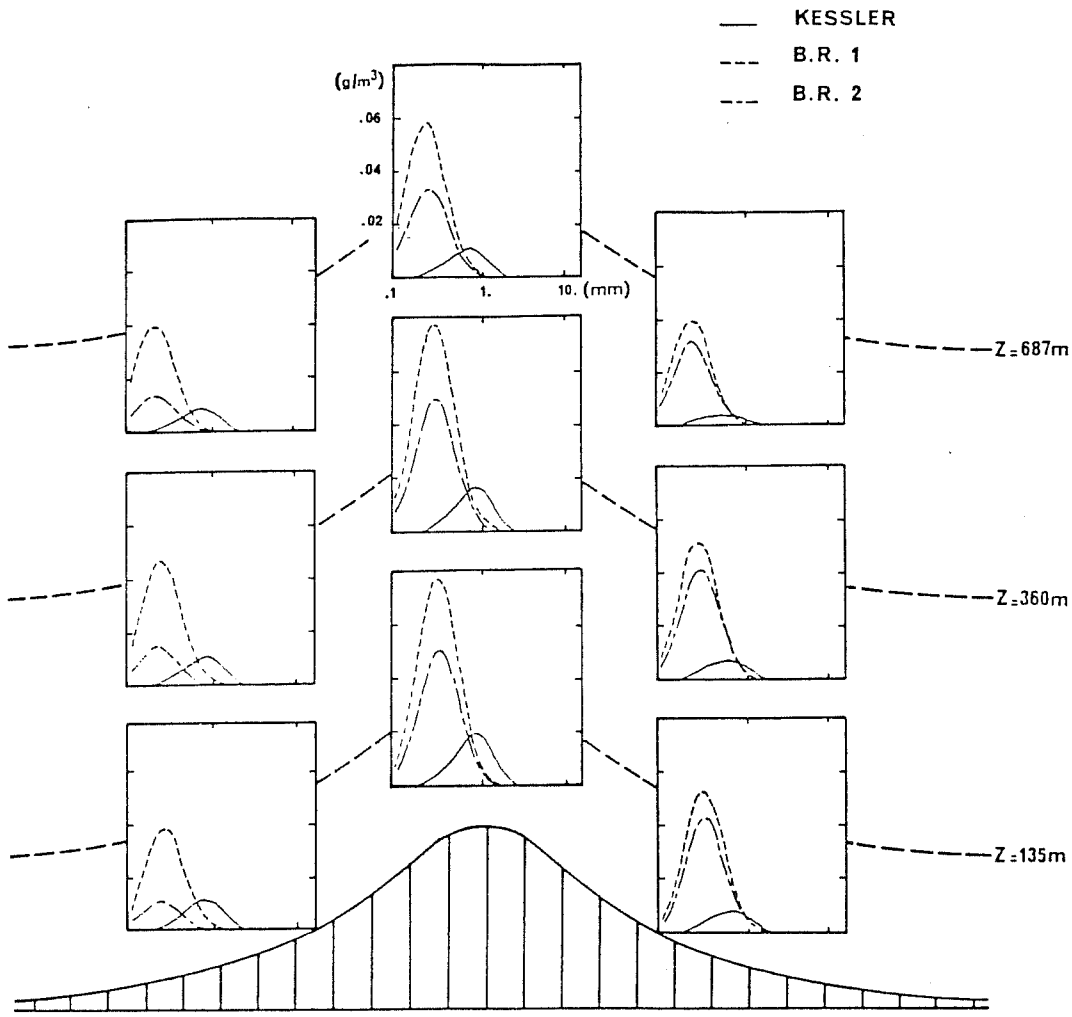

Fig.4 Mass density functions for raindrops, obtained with K, BR1 and BR2 for three grid points located at mountain top, upwind and downwind from mountain top and for three vertical levels in the model.

of the mountain. For all the selected grid points, the Kessler mass density functions are systematically centered over larger diameters. Such differences in raindrop sizes provide a rationale for the interpretation of the differing behavior of the BR and K schemes. In the Kessler scheme, large raindrops precipitate with greater terminal velocity than BR raindrops, so that rainwater mixing ratio is depleted much faster. Another effect directly related to raindrop size is the downwind spreading of the precipitating zone in the case of BR. The BR raindrops which are smaller than the Kessler raindrops, are more sensitive to wind drift effects.

Additional numerical simulations in which the role of each microphysical process was studied individually, permitted the establishment of a hierarchy between the different processes. Sedimentation and accretion both size dependent processes are dominant in determining rainfall production in the two parameterizations; however, their relative contribution differs notably between the two schemes. Other process like self-collection and rain evaporation play a significant role in BR cases by reducing the downwind extent of the precipitating area.

3.2.2 Feeder-seeder cloud

The mountain wave simulations give evidence of the main differences between K and BR but do not enable us to draw any definitive conclusions in favor of one or the other parameterization. Therefore, it is worthwhile to check the results from the two schemes against experimental data. A field study of orographic rain conducted by Hill et al. (1981) over South Wales has been selected for several reasons. First, this experiment is well-documented, combining radar measurements and rain gauge data. Results from these observations showed that the generation of orographic rain is greatly favored by the Bergeron (1965) feeder-seeder mechanism, according to which raindrops from upper level (seeder) clouds wash out small droplets through accretion within low-level (feeder) clouds formed over the hill.

We have simulated the eight events presented by Hill et al. (1981). Some of the events were subdivided according to the low-level windspeed v_L, yielding a total of fourteen cases. These cases are listed in Table 1 together with the seeding height z_s and the precipitation rate at seeding level P_s. Further details can be found in Richard et al. (1987). The model is initialized for each case with the corresponding radiosounding taken from Hill et al.(1981). The terrain is represented by a slope of 1 in 40 leading to a 400 m high plateau. The model is run over the fourteen seeding events with K,

BR1 and BR2, defined exactly as for the mountain wave simulations. In each case, the orographic enhancement of the surface rainfall rate is computed as the difference between the precipitation rate at the hill crest, P_h, and the precipitation rate at the coast, P_o.

Table 1 Computed cases for the observations of Hill et al. (1981).

Case no.	v_L (ms^{-1})	z_s (km)	P_s (mmh^{-1})
1	30	2.2	2.5
2	28	1.5	1.5
3*a*	23	1.5	1
3*b*	26	1.5	1
4*a*	16	1.5	1
4*b*	22	1.5	1
4*c*	26	1.5	1
5	21	1.5	1
6*a*	19	1.5	1
6*b*	17	1.5	1
7*a*	14	1.5	1.5
7*b*	18	1.5	1.5
7*c*	21	1.5	1.5
8	14	1.5	3

Figure 5 presents the computed enhancements from coast to hill versus the observed values for all cases. Figures 5a, 5b and 5c correspond respectively to computations with the K, BR1 and BR2 parameterizations. The best agreement between computations and observations is found for the BR1 parameterization. BR2 does not give results as good as BR1 and shows a slight tendency to underestimate the enhancement. In the case of the BR parameterizations, the best fit to the observed data is obtained for the most maritime case BR1. The agreement with observations was even better with a more maritime cloud spectrum (σ_c= 0.28; $\overline{D_c}$ = 40μm) as simulated in Richard et al. (1987). However, the difference between the two BR parameterizations is not as large as the difference between the K and BR schemes. With Kessler, the enhancement is globally underpredicted especially in the case of strong low-level windspeeds (cases 1, 2, 3, 4b and 4c). Figure 6 shows the precipitation enhancement

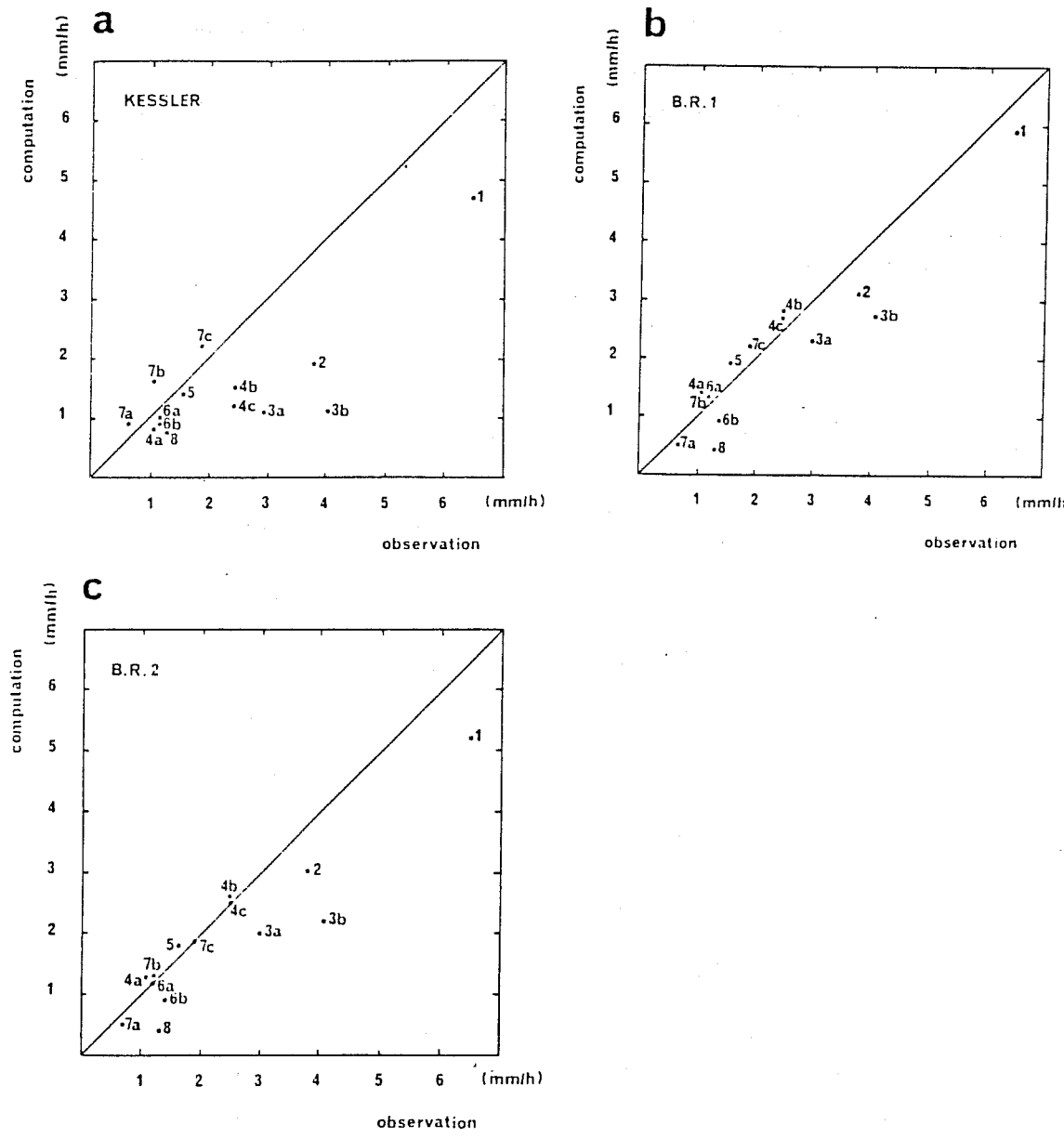

Fig.5 Computed orographic enhancement $P_h - P_o$ versus the observed value for the fourteen cases of Hill et al. (1981); (a) for K; (b) for BR1 and (c) for BR2 parameterizations.

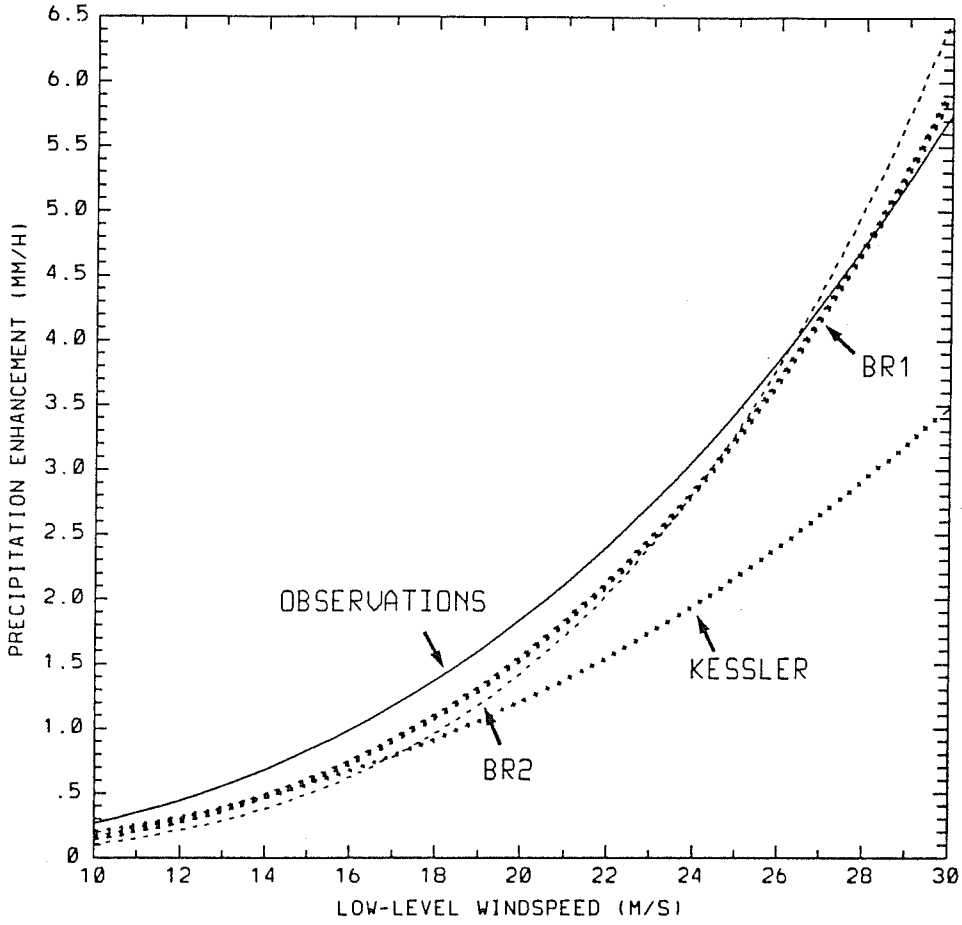

Fig.6 Precipitation enhancement as a function of low-level windspeed for the observations and for the computations with K, BR1 and BR2.

as a function of the low-level windspeed for the observations and the three computations. All the parameterizations approximately depict the enhancement in the speed range of 10 to 20 m s^{-1}. For stronger wind values, large discrepancies appear between observations and the Kessler results. Only the BR parameterizations are able to reproduce the observed dependency of the orographic enhancement on the low-level windspeed.

4. EXAMPLES OF RESULTS

In order to now illustrate the impact of an explicit cloud and precipitation scheme on the dynamics of mesoscale systems, we present some results corresponding to the simulation of different meteorological situations on the β or α-mesoscale. The first case is an academic mountain wave situation over a two-dimensional bell-shaped mountain. The second case is a simulation of an Eady wave in a moist atmosphere. The last example corresponds to a three-dimensional case study of frontogenesis taken from the FRONT87 field experiment.

4.1 2D mountain wave

Let us consider an idealized atmosphere of constant static stability ($N = 0.0132s^{-1}$), constant windspeed ($\overline{u}$ =10 ms^{-1}) and constant relative humidity ($H = 99\%$), impinging a two-dimensional bell shaped mountain of 20km half-width and 250m height. Under such conditions, where the Scorer parameter is constant with height, a vertically propagating wave is expected to develop with a vertical wave length of $2\pi\overline{u}/N$ i.e. 4760m. For these simulations, the model was run over a domain of 100 grid points on the horizontal (with a grid size of 5km) and 61 levels on the vertical.

Four experiments have been performed using different the different types of explicit formulations mentioned in section 2. In the first experiment, considered as the control run, condensation was not allowed, and moisture was considered only as a passive tracer. In the second experiment, condensation was allowed but the formation of precipitation was inhibited making this way the condensation/evaporation process fully reversible. In the third experiment, all the condensed liquid water was assumed to fall out instantly and finally in the fourth experiment, cloud and rain were fully represented by the Berry-Reinhardt parameterization.

The results corresponding to these 4 simulations are shown after 24 hours of integra-

tion, i.e; an adimensional time of 43.2. The inverse Froude number $Fr^{-1} = Nh/\overline{u}$ has a value of 0.33, indicating that the wave response will be weakly non linear. The perturbations of the wind field (amplified by a factor 4), are shown in Fig.7. The shaded areas correspond to the cloudy areas when a cloud stage is activated. The comparison of the first two simulations clearly shows that condensation considerably damps the amplitude of the perturbations. The vertical wave length is also significantly modified. The first simulation reproduces the theoretical adiabatic value of 4.7 km while the second simulation shows a wave length of 5.2 km. In the cases with precipitation, although the perturbations remain much weaker than in the control case, they are slightly stronger than in the second simulation. The main difference is located in the low levels where the zone of strong wind has a larger downwind extend. This behaviour is more pronounced in the case of instant rainout compared to the Berry-Reinhardt case. The interpretation of these results directly derives from the modification of static stability induced by the condensation process. In an atmosphere with constant wind and constant stability, the fields perturbations are proportional to the Brunt-Väisälä frequency, which is considerably reduced in the saturated zones. The non-saturated value, $N = 0.0132s^{-1}$, is lowered to a value of $0.007s^{-1}$ near the ground, as soon as condensation occurs. By looking at the cloud fields associated to the simulations 2 and 4, it is not surprising to obtain for these cases a wave of weaker amplitude. It is also interesting to notice that when the precipitation is taken into account, the shape of the low level cloud becomes more realistic. The cloud droplets are washed out by the precipitating drops before reaching the lee slope of the mountain as it was the case for the second simulation.

Some additional information can be obtained by looking at the vertical profiles of the momentum fluxes. These profiles have been reported in Fig.8a, after being normalized by their theoretical adiabatic values. As expected, the control run profile is constant with height (at least in the region of the computational domain located below the absorbing layer). The value slightly greater than 1, is indicative of the quasi-linear response. When the reversible condensation/evaporation process is taken into account, the momentum flux value is halved, but the profile still remains constant with height. On the other hand, when precipitation are allowed, there is net heating and the vertical profile shows higher values in the lowest levels where the precipitation occurs. It is worth noting that an instant rainout parameterization significantly overestimates this effect, thus leading to a surface value even stronger than the value obtained in the adiabatic control case. This becomes more evident when considering the time evolution of the surface pressure drag, plotted on Fig.8b, which can be considered as

NO CONDENSATION
NO PRECIPITATION

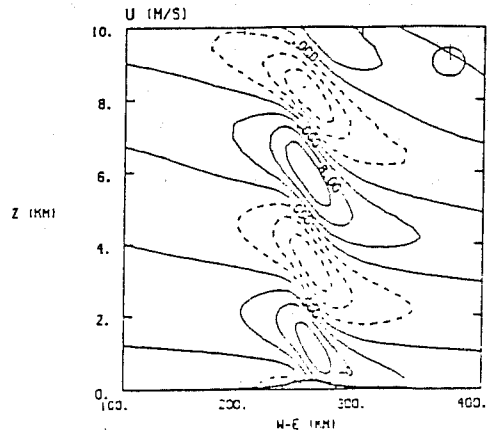

CONDENSATION
NO PRECIPITATION

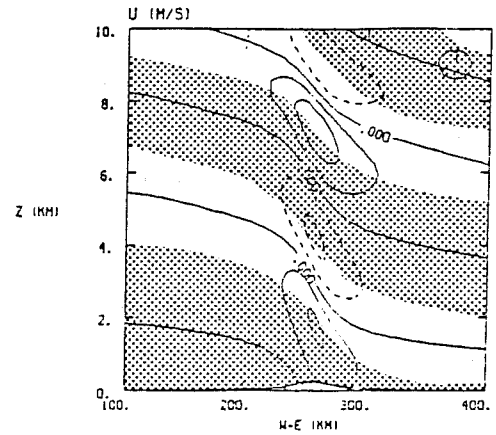

PRECIPITATION:
INSTANT FALL OUT

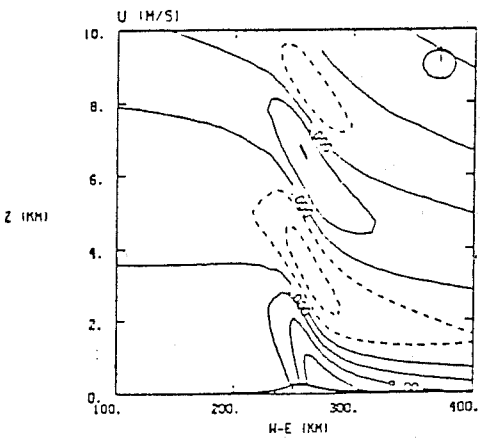

PRECIPITATION:
BERRY-REINHARDT

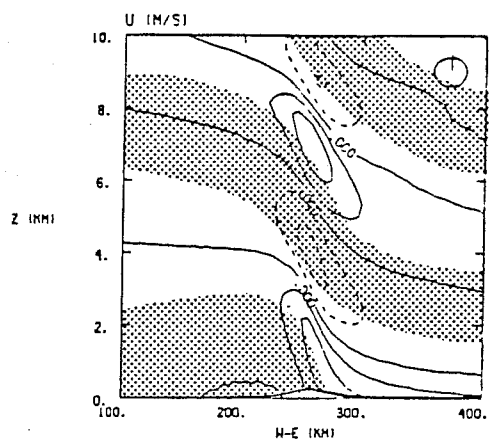

Fig.7 Wind field perturbations amplified by a factor of 4. The shaded area corresponds to the outer contour of the cloud.

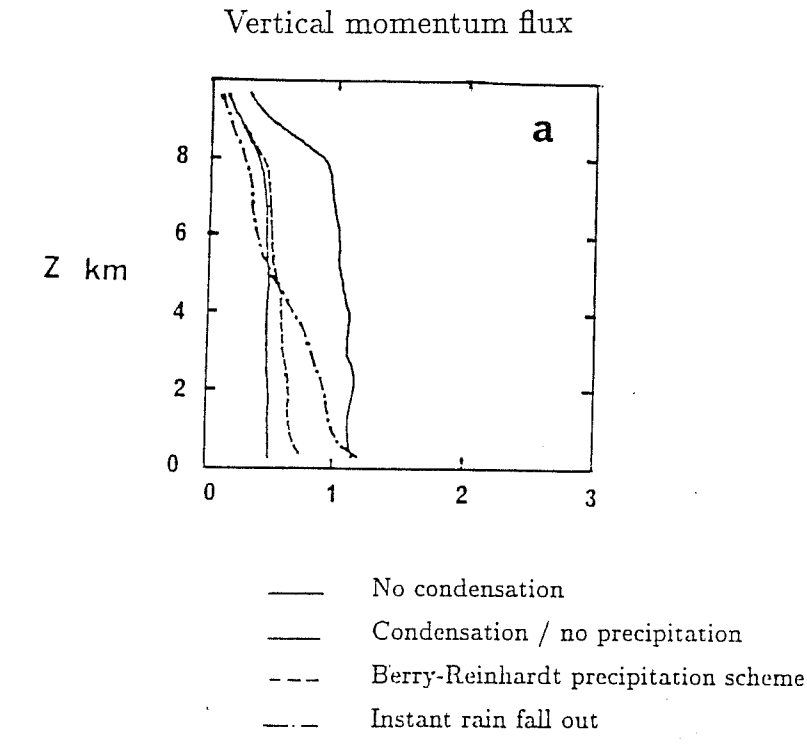

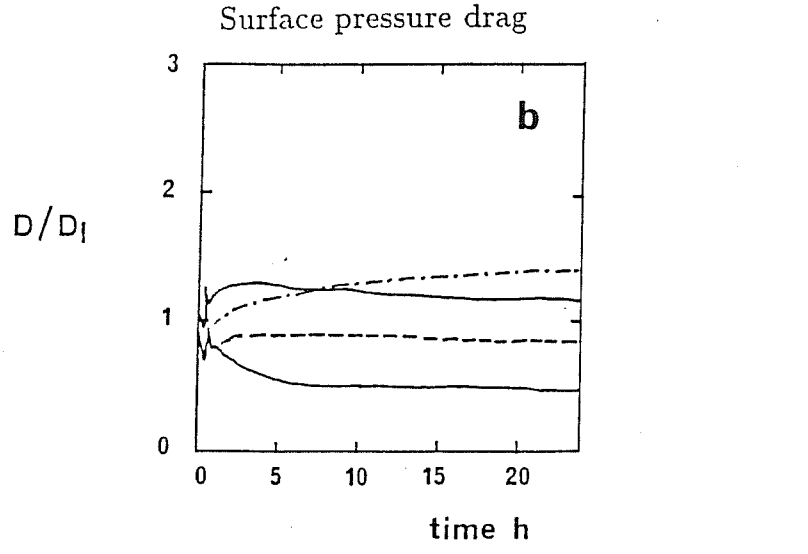

Fig.8 a) Vertical profiles of the momentum flux normalized by its adiabatic value. b) Time evolution of the normalized surface pressure drag.

an indicator of the wave activity. One finds again the same results, i.e. condensation damps the wave amplitude but at a rate controlled by the presence of precipitation. The curve relative to the last simulation indicates that a very crude representation of the precipitating process, can lead to a wrong result i.e a fictitious increase of the surface pressure drag attributed to the net heating resulting from the precipitation.

4.2 Eady wave

Numerical simulations of frontogenesis in a moist atmosphere have been performed with the same model, initialized with the solution of the analytical model of an Eady wave due to Hoskins and Bretherton (1972). A geostrophic shearing deformation field is used to force the development of a 2D baroclinic wave in which a cold front is formed (Keyser and Anthes, 1982). The model was run with 82 grid points in the x direction with a grid size of 40 km and 15 vertical levels. The coordinate system was moving toward the East with a constant phase speed (14.35m/s) of the analytical wave. The horizontal domain was equal to the analytical wavelength (3247km). The zonal boundary conditions were periodic and the longitudinal gradients were zero except for the potential temperature. The parameterization of the planetary boundary layer was based upon the prediction of the turbulent kinetic energy as described in Mahfouf et al. (1987).

Four experiments have been performed, the first one without moisture, for reference and comparison with other studies, and the three others using respectively the type I,II and III of explicit heating representation. The corresponding fields of vertical velocity obtained after 24h of integration have been reported in Fig.9. The reference case reproduces the results obtained by Keyser and Anthes (1982). When only PBL physics is included (Fig.9a), an ascending vertical jet arises in the atmospheric boundary layer ahead of the front, due to horizontal convergence forced by surface friction. When precipitation and PBL physics are both considered, the strong frictional induced low level ascending motion ahead of the front is found to occur in conjunction with updrafts associated with pre-frontal rainbands and downdrafts caused by evaporative cooling. The results of the last simulation (Fig.9c) are quite similar to Hsie et al., (1984) results and they realistically reproduce some of the observed features associated with front in a moist atmosphere like a banded convective structure propagating away from the cold front. In case of instant rain parameterization (Fig.9b), the intensity of the first mid level updraft and downdraft is much stronger than in

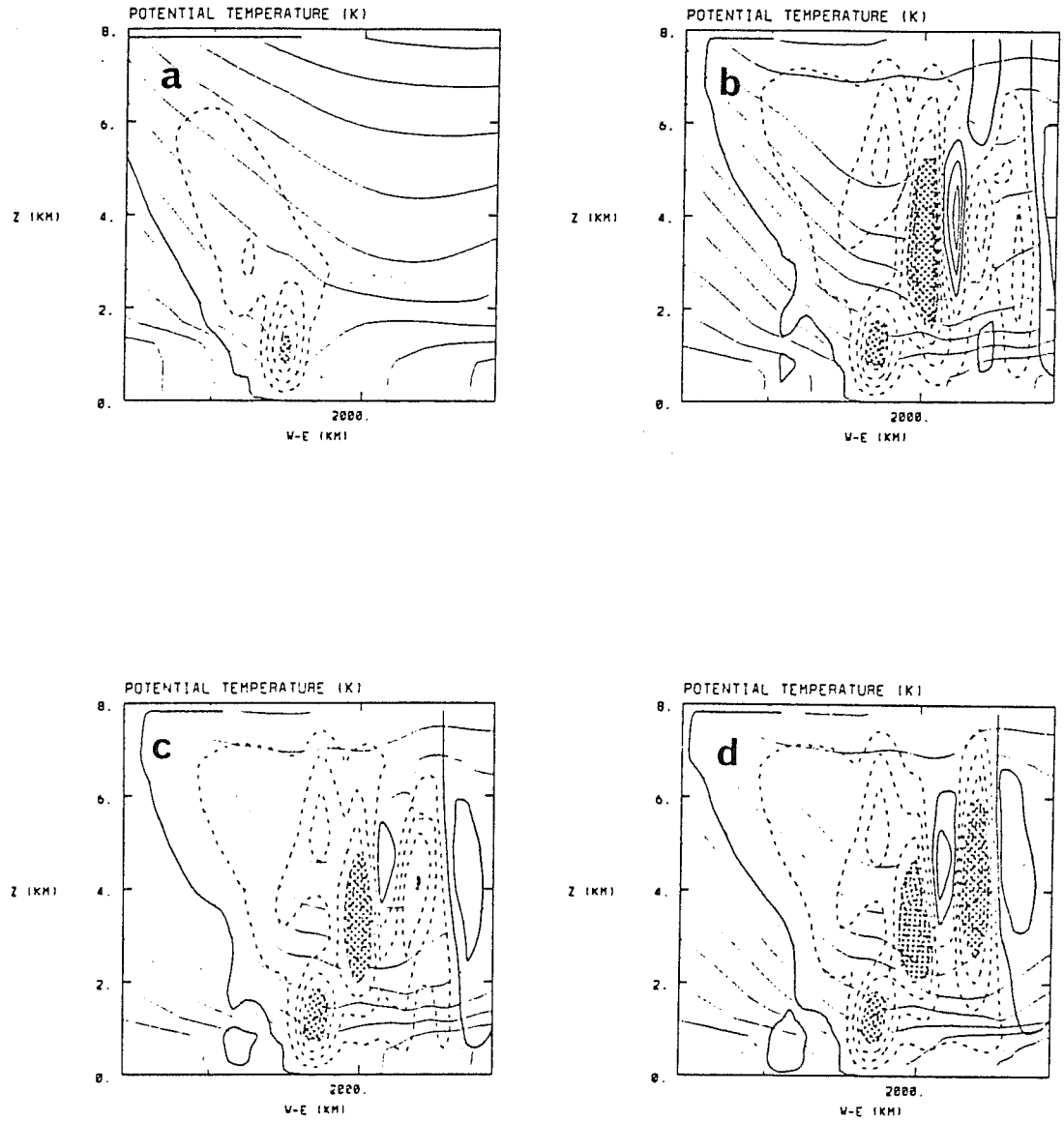

Fig.9 Vertical velocity fields (in hPA/h) after 24h of integration superimposed to the potential temperature fields for a) dry simulation b) a type I explicit condensation (instant rain out), c) a type II, d) a type III (Kessler parameterization). The shaded areas correspond to updrafts greater than 40 hPa/h.

the two other moist cases. The inclusion of a cloud stage (Fig.9c) weakens both the updraft and downdraft.When rain is then incorporated (Fig.9d) the first downdraft is reinforced by the evaporative cooling as well as the next ascending branch.

4.3 IOP2 of FRONT87

The meteorological situation of the IOP2 of the field experiment FRONT87 has been simulated with the model. The size of the domain was 2400x2400 km^2 with a grid size of 40 km. The model was run with 30 vertical levels. The model was initialized for this case with the analysis provided by the French Meteorological Service for the numerical weather forecasting model Péridot.

Two experiments have been performed, one with the explicit precipitation scheme (Kessler) only and the second one with the implicit convective scheme (Bougeault, 1985) only. The impact of each scheme on the dynamics of the frontal system is illustrated in Fig.10, where are plotted for each case the horizontal gradient of the equivalent potential temperature at 850hPa. The warm front is almost insensitive to a change of the precipitation scheme. The main discrepancy between the two simulations occurs in the vicinity of the cold front. In the case of explicit condensation, the undulation of the cold front is more pronounced and a banded structure clearly appears.

The corresponding precipitation rates are plotted in Fig.11. The precipitation associated with the warm front are only produced by the explicit scheme while the cold sector precipitation occurs only in the case of the convective scheme. Both schemes give their maximum rainfall along the cold front but with very different patterns.

Further investigations need to be done on this case study, but one of the preliminary conclusion will be that both schemes are probably necessary in order to reproduce the complete precipitation pattern.

5. CONCLUSION

Two detailed explicit schemes for calculating cloud water and precipitation water have been described and compared under various conditions of orographically forced rainfall at the β mesoscale. In the case of feeder-seeder cloud systems, involving intricate microphysical processes, the more complete Berry and Reinhardt parameterization gave better results than the Kessler one.

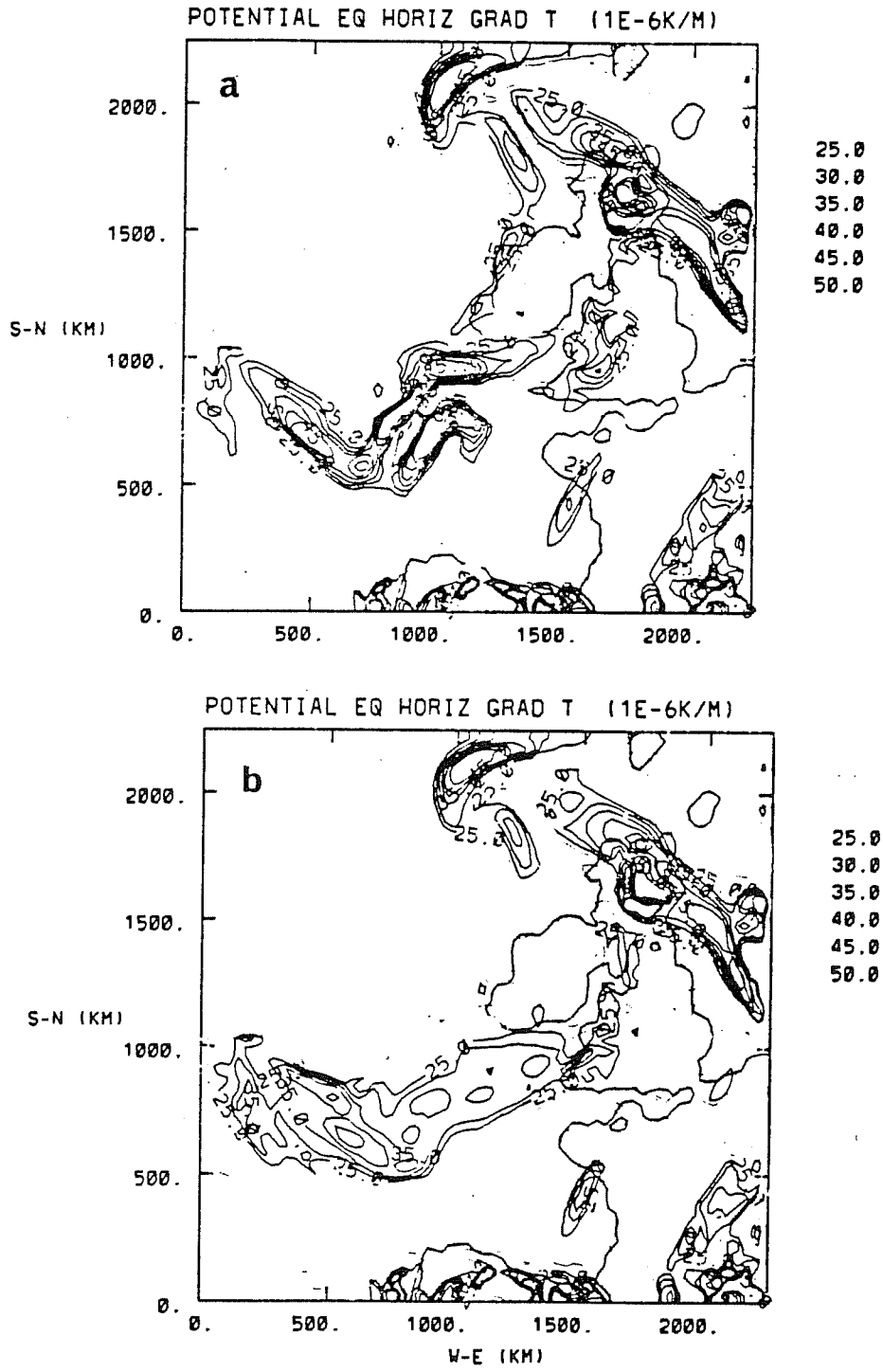

Fig.10 Horizontal gradient of equivalent potential temperature after 6h of integration (18:00, 11 November 1987) for a) a simulation with explicit condensation (Kessler), b) a simulation with an implicit convective scheme (Bougeault).

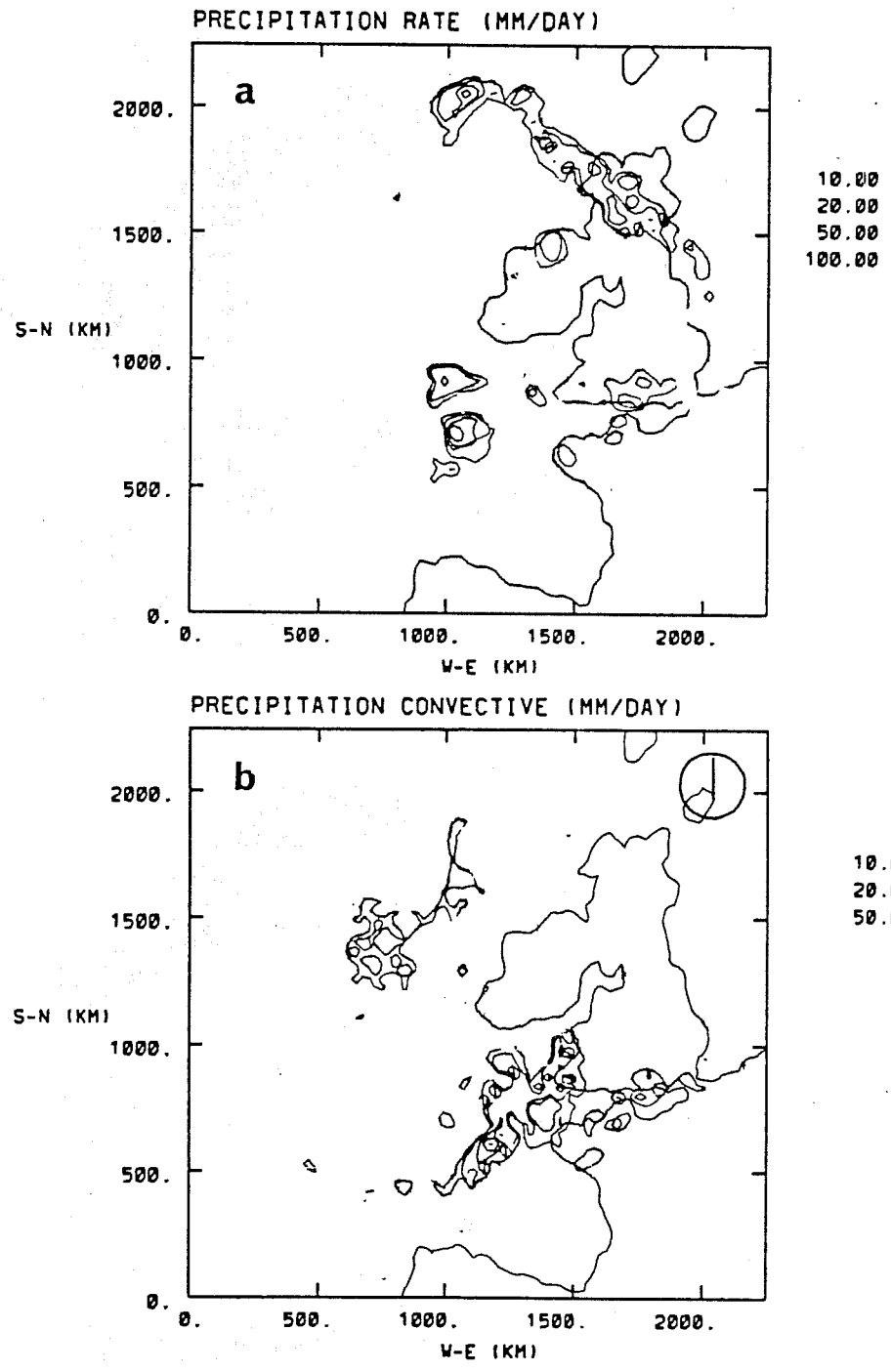

Fig.11 Precipitation rates after 6h of integration (18:00, 11 November 1987) for a) a simulation with explicit condensation (Kessler), b) a simulation with an implicit convective scheme (Bougeault).

Various simplifications of these two schemes have been then considered for meso-α and meso-β scale. The instant rainout assumption was found to significantly alter the vertical motion for both the mountain wave situation and the moist frontogenesis case.

Finally a preliminary simulation of the IOP2 of the FRONT87 experiment showed that a complete description of the frontal precipitating system could not be obtained without both the explicit condensation scheme and the implicit convective scheme.

This study was mainly focussed on the impact of cloud and precipitation schemes in the case of strong mesoscale forcing occurring for orographically driven flows and frontogenesis. However, a detailed explicit microphysical scheme might be necessary as well to describe the complex interactions occurring between turbulence, radiation and eventually physico-chemistry in the case of large scale stratus cloud for instance.

ACKNOWLEGMENTS

The authors would like to express their gratitude to Prof. R.Rosset and Dr. E.C. Nickerson for their valuable contribution. P. Bougeault is thanked for his help in using the convection scheme. The figures relative to the simulation of FRONT87 were kindly provided by J.L Sortais and X.-D. Yu. This work was supported by funds from Electricité de France. Computer resources were provided by ECMWF, CCVR and Météo-France.

REFERENCES

Anthes, R.A., Y.H. Kuo and J.R. Gyakum, 1983: Numerical simulations of a case of explosive marine cyclogenesis. Mon.Wea.Rev., 111, 1174-1188.

Bergeron, T., 1965: On the low-level redistribution of atmospheric water caused by orography. Suppl.Proc.Int.Conf.Cloud Phys., Tokyo, 96-100.

Berry, E.X., and R.L. Reinhardt, 1974a: An analysis of cloud drop growth by collection: Part II. Single initial distributions. J.Atmos.Sci., 31, 1825-1831.

Berry, E.X., and R.L. Reinhardt, 1974b: An analysis of cloud drop growth by collection: Part III. Accretion and Self-collection. J.Atmos.Sci., 31 , 2118-2126.

Bougeault, P., 1985: A simple parameterization of the large scale effects of cumulus convection. Mon.Wea.Rev., 113, 2108-2121.

Chaumerliac, N., E. Richard, J.-P. Pinty, and E. C. Nickerson, 1987: Sulfur scavenging in a mesoscale model with quasi-spectral microphysics : Two-dimensional results

for continental and maritime clouds. J.Geophys.Res., 92, 3114-3126.

Davies, H.C., 1983: Limitations of some common lateral boundary schemes used in regional NWP models. Mon.Wea.Rev., 111, 1002-1012.

Durran, D.R., and J.B. Klemp, 1983: A compressible model for the simulation of moist mountain waves. Mon.Wea.Rev., 111, 2341-2361.

Feingold, G., and Z. Levin, 1986: The lognormal fit to raindrop spectra from frontal convective clouds in Israel. J.Climate.Appl.Meteor., 25, 1346-1363.

Hill, F.F., K.A. Browning and M.J. Bader, 1981: Radar and raingauge observations of orographic rain over south Wales. Quart.J.Roy.Meteor.Soc., 107, 643-670.

Hoskins, B.J and F.P. Bretherton., 1972: Atmospheric frontogenesis models: Mathematical formulation and solution. J.Atmos.Sci., 29, 11-37.

Hsie, E. and R.A. Anthes, 1984: Simulations of frontogenesis in a moist atmosphere using alternative parameterizations of condensation and precipitation. J.Atmos.Sci., 41, 2701-2716.

Hsie, E., R.A. Anthes and D. Keyser, 1984: Numerical simulation of frontogenesis in a moist atmosphere. J.Atmos.Sci., 41, 2581-2594.

Kessler, E., 1969: On the distribution and continuity of water substance in atmospheric circulations. Meteor.Monog.,10, N° 32, 84 pp.

Keyser, D. and R.A. Anthes, 1982: The influence of planetary boundary layer physics on frontal structure in the Hoskins-Bretherton horizontal shear model. J.Atmos.Sci., 39, 1783-1802.

Mahfouf, J.F., E. Richard, P. Mascart, E.C. Nickerson and R. Rosset, 1987: A comparative study of various parameterizations of the planetary boundary layer in a numerical mesoscale model. J.Clim.Appl.Meteor., 26, 1709-1722.

Marshall, J.S., and W. McK. Palmer, 1948: The distribution of raindrops with size. J.Meteor., 5, 165-166.

Molinari, J. and M. Dudek, 1986: Implicit versus explicit convective heating in numerical weather prediction model. Mon.Wea.Rev., 114, 1822-1831.

Nickerson, E.C., E. Richard, R. Rosset and D.R. Smith, 1986: The numerical simulation of clouds, rain, and airflow over the Vosges and Black Forest Mountains: A meso-β model with parameterized microphysics. Mon.Wea.Rev., 114, 398-414.

O'Brien, J.J., 1970: A note on the vertical structure of the eddy exchange coefficient in the planetary boundary layer. J.Atmos.Sci., 27, 1213-1215.

Richard, E., N. Chaumerliac, J.F. Mahfouf and E.C. Nickerson, 1987: Numerical simulation of orographic enhancement of rain with a mesoscale model. J.Climate.Appl.Meteor., 26, 661-669.

Richard, E. and N. Chaumerliac, 1989: Effects of different rain parameterizations on

the simulation of mesoscale orographic precipitation. 28, 1197-1212.

Ross, B.B. and I. Orlanski, 1982: The evolution of an observed cold front. Part I. Numerical simulation. J.Atmos.Sci., 39, 296-327.

Waldvogel, A., 1974: The N_o jump of raindrop spectra. J.Atmos.Sci., 31, 1067-1078.

Zhang, D.-L., E.-Y. Hsie and M.W. Moncrieff, 1988: A comparison of explicit and implicit predictions of convective and stratiform precipitating weather systems with a meso-β-scale numerical model. Quart.J.Roy.Meteor.Soc., 114, 31-60.